# Au/Co promoted CeO2 catalysts for formaldehyde total oxidation at ambient temperature: role of oxygen vacancies

Guillaume Rochard, Jean-Marc Giraudon, Leonarda Francesca Liotta, Valeria La Parola, Jean-Francois Lamonier

ARTICLE

# Au/Co promoted $CeO_2$ catalysts for formaldehyde total oxidation at ambient temperature: role of oxygen vacancies

Received 00th January 20xx,
Accepted 00th January 20xx

DOI: 10.1039/x0xx00000x

Guillaume Rochard,[a] Jean-Marc Giraudon,[a] Leonarda Francesca Liotta,*[b] Valeria La Parola,[b] Jean-François Lamonier, *[a]

Au catalysts with loading 1.5 and 3 wt% were dispersed over $CeO_2$ and Co (9; 12 mol%) promoted $CeO_2$, by deposition-precipitation method, followed by calcination at 350°C. The fresh supported Au catalysts were characterized by several techniques in order to investigate their morphological, structural as well as redox properties before to be tested in formaldehyde (HCHO) total oxidation. All the supported Au catalysts exhibit at 25°C HCHO oxidation into $CO_2$ and have a great stability upon time on stream (40 h). While the 3 wt% Au catalysts demonstrate higher HCHO conversion than their low-gold counterparts (1.5 wt% Au), a remarkable improvement of HCHO conversion was observed using Co-promoted ceria (9 mol%). Based on the HCHO amount (in µmol) converted into $CO_2$ per gram of gold per second after 40 h on stream, 1.5Au/CeCo showed the best activity (~ 3.9) as compared to the other catalysts (≤ 2.0). XPS characterization of the fresh catalysts indicates Au species mainly in slightly ionic $\delta^+$ valence state without excluding the possibility of metallic gold. Furthermore, it is found no marked changes in gold dispersion when adding cobalt. Promotion of HCHO oxidation over gold supported on Co-promoted ceria catalysts can be related to a higher oxygen vacancy concentration and an improvement of the redox properties which can contribute to a better activation of $O_2$ and an enhancement of the oxygen mobility.

## Introduction

Formaldehyde (HCHO) is a dangerous volatile organic compound (VOC), mostly used in wood industry as a glue component. Degradation of this glue with time allows the release of HCHO in our indoor environment. It is well known that prolonged exposure to HCHO contributes to important health issues (burning sensation, breath problem, cancers)[1]. This pollutant can be removed from air by several methods such as adsorption and photocatalysis. However, total oxidation by heterogeneous catalysis into harmless species ($CO_2$ and $H_2O$) is the most promising alternative[2]. So far, supported noble metals catalysts such as Pt, Pd and Au have been successfully used for low/room temperature catalytic oxidation of formaldehyde[3-6]. The performance of supported metal catalysts relies on many factors, including metal particle size, dispersion and metal–support interactions, and differentiation of these effects is challenging in order to get an insight in the operating mode of the catalyst. As catalyst, gold was considered as inert until the works of Haruta *et al.*[7] showing highly dispersed gold nanoparticles (NPs) to be very active in CO oxidation. It is commonly reported that dispersion has significant importance for gold activity in VOC removal[8]. However, the dispersion of gold NPs is mostly related to the mode of preparation[9-12], gold loading[13-15] and calcination temperature[14-18]. Among the different materials already used for gold deposition such as hydroxyapatite, fluoroapatite, $SiO_2$, HZSM-5, $Al_2O_3$, $FeO_x$, $TiO_2$, $ZrO_2$ [8,11,14,16,19], $CeO_2$ appears as an attractive material due to its low-temperature redox activity, unusual oxygen storage capacity and the possibility of interacting strongly with gold[20]. It is well known that the electronic and redox properties of ceria are dominated by the presence of oxygen vacancies[21] which are thought to play a major role in catalysis[22]. On purpose T. Sayle *et al.*[23] highlighted the correlation between the low formation energies of surface oxygen vacancies (facilitated on the (110) and (310) planes) and CO oxidation reaction. Thus, the authors predict that any process which preferentially exposed (110) and (310) surfaces enhances activity for CO oxidation. Otherwise X. Liu *et al.*[24] obtained an interesting correlation between the size of oxygen vacancy clusters and the promotion of reducibility and activity of ceria nanorods in CO oxidation reaction.

The oxidation of low concentration formaldehyde in air over $Au/CeO_2$ in HCHO oxidation is well reported[15,25-27]. It turns out that oxygen vacancies play a critical role in HCHO oxidation reaction. With that respect, M. Jing *et al.*[20] found that the oxidation of HCHO is more favourable on $Au/Ce_{1-x}O_{2-y}$ than on $Au/CeO_2$ consistent with a co-adsorption of HCHO and $O_2$ on the defective $CeO_2$ surface. The presence of adsorbed active oxygen species contributed to C-H cleavage and reduced the energetically cost of HCHO oxidation reaction. Q. Xu *et al.*[28] reported on the importance of shape and size control of ceria to get nanorods with {110} and {100} facets which present a

[a] Univ. Lille, CNRS, Centrale Lille, ENSCL, Univ. Artois, UMR 8181 – UCCS – Unité de Catalyse et Chimie du Solide, F-59000 Lille, France.
Jean-François Lamonier : jean-francois.lamonier@univ-lille.fr
[b] Istituto per lo Studio dei Materiali Nanostrutturati ISMN-CNR, Via Ugo La Malfa 153, 90146 Palermo, Italy.
Leonarda Francesca Liotta : leonardafrancesca.liotta@cnr.it

Electronic Supplementary Information (ESI) available: [details of any supplementary information available should be included here]. See DOI: 10.1039/x0xx00000x

relatively low energy for oxygen vacancy formation. Furthermore, H. F. Li *et al.*[29] reported on the beneficial role of high surface area of ceria allowing to provide a high density of oxygen vacancies and on the presence of high oxidation states of gold through the formation of a $Au_xCe_{1-x}O_{2-\delta}$ solid solution as potential centres for HCHO adsorption.

In order to get more efficient catalysts in HCHO oxidation one possible strategy can be to dope ceria with another transition metal (TM) through the research of a synergetic effect between the two TM oxides allowing a better activation of the Au species and a better mobility of the active oxygen species on the catalyst surface.

In that way, the performances of Au-$CeO_2$-$Co_3O_4$ based catalysts were investigated in HCHO oxidation[30,31]. B. Liu *et al.*[31] reported 100 % HCHO conversion into $CO_2$ at a temperature of about 39°C over a three-dimensionally ordered macroporous (3DOM) Au/$CeO_2$-$Co_3O_4$ more performant than a 3DOM Au/$CeO_2$. A synergetic effect between $Co_3O_4$ and $CeO_2$ through the participation of $Co_3O_4$ in the oxygen transfer during the HCHO catalytic oxidation process was proposed by the authors to account for such a behavior.

In this paper we present a novel approach for the synthesis of Au/$CeO_2$-$Co_3O_4$ catalysts based on the dispersion of gold (1.5 and 3 wt%) by deposition-precipitation (DP) over Co-promoted ceria (Co : 9 and 12 mol%) and un-promoted ceria synthesized by hydrothermal method. Both catalytic reactivity and stability of the as-prepared samples toward HCHO oxidation were examined. The fresh catalysts were characterized extensively by XRD, Raman, $N_2$-physisorption, $H_2$-TPR, XPS and ToF-SIMS. HRTEM images were registered for two selected catalysts. The catalytic performances were discussed in terms of oxygen vacancies effect.

## EXPERIMENTAL DETAIL

**Material synthesis:** Cerium based oxides were prepared *via* the hydrothermal method, adapted from Q. Xu *et al.*[28]. Typically, for pure ceria preparation, 6 g of $Ce(NO_3)_3.6H_2O$ (Aldrich, 99 %) were dissolved in 30 mL of $H_2O$ and 40 mL of NaOH (2.5 $mol.L^{-1}$ ; Aldrich, > 98%) were added to the solution under vigorous stirring. The resulting suspension was rapidly transferred into a 100 mL Teflon autoclave and heated in an oven at 120 °C for 23 h. The aged precipitate was collected by filtration, washed with deionized water until neutrality and finally with ethanol. The resulting powder was dried overnight at 60 °C and calcined at 350°C for 3 h (heating rate 2°C.$min^{-1}$). This sample was denoted Ce.

For Co-promoted ceria preparation, the same experimental procedure was used except that an appropriate amount of $Co(NO_3)_2.6H_2O$ (Aldrich, 99 %) was simultaneously added with the cerium(III) nitrate into 30 mL of $H_2O$. Those samples were denoted CeCox with x = 9 or 12, x expressing the Co molar percentage.

For the synthesis of Au based catalysts, an appropriate volume of $HAuCl_4.3H_2O$ (0.01 $mol.L^{-1}$; Aldrich, 99.999 %) was added to an aqueous suspension of the ceria based support and kept under stirring for 1 h. At that stage, the pH of the solution was fixed at ~ 7.5-8.0 by adding $K_2CO_3$ (0.05 $mol.L^{-1}$ ; Aldrich > 99%) and the temperature was allowed to increase to 65 °C. The suspension was kept under stirring overnight. After filtering and careful washing with hot (50 °C) deionized water, the powder was dried overnight at 80 °C before to be calcined at 350 °C for 2 h (heating rate 2 °C.$min^{-1}$). Those samples were denoted yAu/CeCox with y = 1.5 or 3, y expressing the Au weight percentage.

**Material Characterization:** $N_2$ adsorption-desorption isotherms were measured at liquid nitrogen temperature, using a gas adsorption analyser (TriStar II 3020). The sample was heated at 100°C for 3 hours under vacuum before measurement. Pore volume was determinate at $P/P_0$ = 0.99. The BET method was used to calculate the specific surface areas. Barrett-Joyner-Halenda (BJH) model was used to estimate the pore size distributions.

XRD measurements were carried out with a Bruker D5000 vertical goniometer equipped with Cu anode (Kα radiation λ=1.5418 Å) and a graphite monochromator. A proportional counter and a 0.05° step size in 2θ were used. The integration time was 10 seconds per step and the scan range was from 20 to 80° in 2θ. The assignment of the various crystalline phases was based on the comparison with files in ICSD card (Inorganic Crystal structure data base). The mean crystallite size (d) of $CeO_2$ phase was calculated from the line broadening of the most intense reflection (111) using the Scherrer equation.

HR-TEM characterization of the catalysts was performed using a TECNAI transmission electron microscope (TEM) operating at an accelerating voltage of 200 kV. The prepared powders were deposited onto a carbon-coated copper grid for TEM observation.

The Raman spectra were recorded with a XY800 Raman Dilor spectrometer equipped with an optical multichannel detector (liquid nitrogen-cooled charge coupled device). The 647.1 nm excitation line of a Spectra Physics ion laser with very low power (3 mW) was focused on the compounds using the macroscopic configuration. LABSPEC software allows us to realize acquisitions and data process. Micro-Raman spectroscopy measurements were also performed with a Horiba Jobin-Yvon Labram infinity instrument, equipped with liquid nitrogen cooled CCD detector. The Raman spectra were recorded at λ = 532 nm with a laser power of 0.6 mW. Spectra were recorded in *ex-situ* mode at room temperature in ambient air. The $I_{DEF}/I_{F2g}$ ratio was determined using the following procedure. The area of the $F_{2g}$ component was first extracted from the area of the half-peak positioned on the low Raman shift. The DEF component was deduced from the difference between the total area of the envelope and that of the F2g component.

Redox properties of the samples were evaluated using a conventional temperature-programmed reduction apparatus (Micromeritics model AutoChem II) which monitored the hydrogen consumption of the catalyst sample. 50 mg of the sample was placed in a quartz reactor and heated in flowing air (50 mL.$min^{-1}$) at 150 °C for 0.5 h and then cooled down to 20 °C. Then the reactor was heated from 20 °C to 1000 °C with a

heating rate of 10 °C $min^{-1}$ in a gas mixture (5 vol.% $H_2$ + 95 vol.% Ar, 50 mL.$min^{-1}$).

The X-ray photoelectron spectroscopy (XPS) analyses were performed with a VG Microtech ESCA 3000Multilab, equipped with a dual Mg/Al anode. The unmonochromatized Al Kα radiation (1486.6 eV) was used as excitation source. The sample powders were analyzed as pellets, mounted on a double-sided adhesive tape. The pressure in the analysis chamber was in the range of $10^{-8}$ Torr during data collection. The binding energies (BE) of the different core levels were referred to the Ce $u^{iii}$ component associated to the Ce $3d_{3/2}$ component set at 916.7 eV. Rapid scans of the Ce 3d region were performed before each analysis in order to evaluate the $Ce^{3+}$ percentage avoiding possible $Ce^{4+}$ reduction under the beam[32]. Analyses of the peaks were performed with the software CasaXPS. Atomic concentrations were calculated from peak intensity using the sensitivity factors provided with the software. The BE values are quoted with a precision of ± 0.15 eV and the atomic percentage with a precision of ± 10%.

ToF-SIMS data were acquired using a ToF-SIMS[5] spectrometer (ION-TOF GmbH Germany) equipped with bismuth liquid metal ion gun (LMIG). The samples were bombarded with pulsed $Bi_3^+$ primary ion beam (25 keV, 0.25 pA) rastered over a 500 μm x 500 μm surface area. With a data acquisition of 100 s, the total fluence does not amount up to 1012 ions/$cm^2$ ensuring static conditions. Charge effects were compensated by means of a 20 eV pulsed electron flood gun. Data were collected over a mass range m/z = 0-1200 for both positive and negative secondary ions. The fragments were identified by their exact mass, coupled with the appropriate intensities for the expected isotope pattern.

**Catalytic performances:** The catalytic oxidation of formaldehyde was performed in a fixed-bed reactor (internal diameter = 10 mm) loaded with the catalyst. Before each test, the catalyst was pre-treated 1 hour at 300°C under $O_2$ (20 vol.%)/$N_2$ flow (100 mL.$min^{-1}$) to remove water and surface impurities. Gaseous formaldehyde was generated from para-formaldehyde in a permeation tube placed in a permeation chamber (Dynacalibrator, VICI Metronics Inc.). By adjusting the gas carrier flow ($O_2$ (20 vol.%)/$N_2$) at 100 mL.$min^{-1}$ and the chamber temperature at 100 °C, a stable formaldehyde concentration of 100 ppmv was generated. After pre-treatment, the reactive flow was flushed on the catalyst at 300°C for one hour and the temperature was then allowed to decrease from 300°C to 40°C (0.5°C.$min^{-1}$ until 100°C and 0.2°C.$min^{-1}$ until 40°C) when using free-Au catalysts. Regarding Au based catalysts, the temperature was allowed to decrease from 300°C to 100 °C in air.

At that stage the reactive mixture was introduced in the reactor and after 1 hour under that mixture, the temperature was allowed to decrease from 100°C to 25°C (0.2°C.$min^{-1}$). The catalysts were then treated 1 hour at 25°C in dry air keeping the same operating parameters ([HCHO] : 100 ppmv, total flow rate : 100 mL.$min^{-1}$). The following test of durability was performed for 40 h at 25°C.

The HCHO oxidation tests were performed over 200 mg (free-Au based catalysts) or 100 mg (Au based catalysts). The effluent gases were analyzed online with a Varian CP-4900 Micro-GC equipped with a thermal conductivity detector and COX type column (1m). The formaldehyde conversion ($X_{HCHO}$, %) was evaluated using the following equation :

$X_{HCHO}(\%) = 100 \times [CO_2] / [HCHO]_{ini}$

$[CO_2]$ being the concentration of $CO_2$ at time t and $[HCHO]_{ini}$ being the initial concentration of formaldehyde.

## Results and discussion

### Textural properties

$N_2$ adsorption-desorption isotherms of the supports are shown in Figure S1a. The based ceria samples show isotherms of type IV with a narrow hysteresis loop for Co-promoted ceria ($P/P_0$ = 0.85 to 1 compared to $P/P_0$ = 0.9 to 1 with Co-free ceria). After Co addition, it is found a decrease by about 25% of the SSA compared to pure ceria (Table 1) accompanied by pore size distribution enlargement, while the pore volumes keep unchanged. These results may suggest that cobalt addition affects the morphology of ceria. It is generally reported in the literature that when transition metals ions were promoted in the ceria structure, the SSA increased because of the decrease in the crystallization of metal promoted cerium based oxides[33,34]. Based on our results, it can be proposed that small particles of cobalt oxides are formed at the $CeO_2$ external surface, contributing to the SSA decrease. Au introduction on the supports did not significantly change the isotherms shape (Figure S2a). For same support composition the porous volume and average pore size are slightly decreased without significant variation in SSA values (Table 1). This suggests that well dispersed gold nanoparticles are present at the support surface.

Table 1 : Textural and structural properties of Ce, CeCox and yAu/CeCox samples

| Sample | $S_{BET}$ /$m^2.g^{-1}$ | Pore Volume /$cm^3.g^{-1}$ | Average pore size /nm | d($CeO_2$) /nm | $I_{DEF}/I_{F2g}$* |
|---|---|---|---|---|---|
| Ce | 111 | 0.50 | 20 | 10 | 0.10 |
| CeCo9 | 82 | 0.54 | 32 | 12 | 0.33 |
| CeCo12 | 89 | 0.56 | 32 | 13 | 0.42 |
| 1.5Au/Ce | 116 | 0.42 | 13 | 10 | 0.38 |
| 3Au/Ce | 107 | 0.38 | 15 | 10 | 0.51 |
| 1.5Au/CeCo9 | 79 | 0.44 | 24 | 12 | 0.50 |
| 3Au/CeCo9 | 80 | 0.41 | 22 | 12 | 0.55 |
| 3Au/CeCo12 | 85 | 0.44 | 19 | 13 | 0.58 |

* $I_{DEF}$ corresponds to the intensity of the Raman lines due to ceria defect (> 470 $cm^{-1}$)

### Structural properties

The XRD patterns of the different samples are shown in Figure 1. The peaks at 2θ = 28.5°, 33.0°, 47.4°, 56.2°, 59.0°, 69.4°, 76.6° and 79.0° correspond to the diffraction from (111), (200), (220), (311), (222), (400), (331) and (420) planes of fluorite $CeO_2$ structure, respectively (JCPDS PDF n° 34-0394). After doping

with cobalt, the XRD patterns are quite similar to pure ceria. The $CeO_2$ diffraction peaks are not shifted and the average crystallite size of ceria is unchanged (Table 1). It is generally observed that when Co is introduced in $CeO_2$, a gradual ceria peak shift towards higher angle side and decrease in ceria crystallite size occur with Co concentration increase[35,36,37]. This is explained by the incorporation of smaller $Co^{2+}$ and/or $Co^{3+}$ cations into the $Ce^{4+}$ ion sites[38], leading to a decrease in unit cell volume. However to accommodate the change in size, some authors proposed that up to 5 at%, the incorporation of $Co^{2+}$ causes the reduction of $Ce^{4+}$ into $Ce^{3+}$ leading to the reverse observation, ~~that means~~ namely to the increase of crystallite size and lattice parameter[39,40] with shift to lower angles. The decrease in crystallite size is generally accompanied with the increase of specific surface area[37,41]. Conversely, the decrease in specific surface area observed for CeCo9 and CeCo12 samples supports the possible formation of Co containing phase separately to $CeO_2$ crystalline phase. Besides a careful examination of the XRD patterns of the cobalt containing samples small features attributed to the (311) planes of $Co_3O_4$ spinel (JCPDS PDF n° 43-1003) were observed in the $2\theta$ range 35-40° (Figure S3). After deposition of 1.5 wt% of gold, no diffraction peak of metallic Au (JCPDS PDF n° 66-0091) at $2\theta<38.2°$ (111) was detected, suggesting the presence of highly dispersed crystallites. In the case of Au 3wt% a broad feature in correspondence of the Au (111) peak can be noticed, likely due to the higher weight content and or to a slight size increase with respect to the 1.5 wt% (Figure S3). Due to the low intensity and partial overlapping of the Au (111) and $Co_3O_4$ (222) peaks, it is not straightforward to evaluate the Au crystallite size.

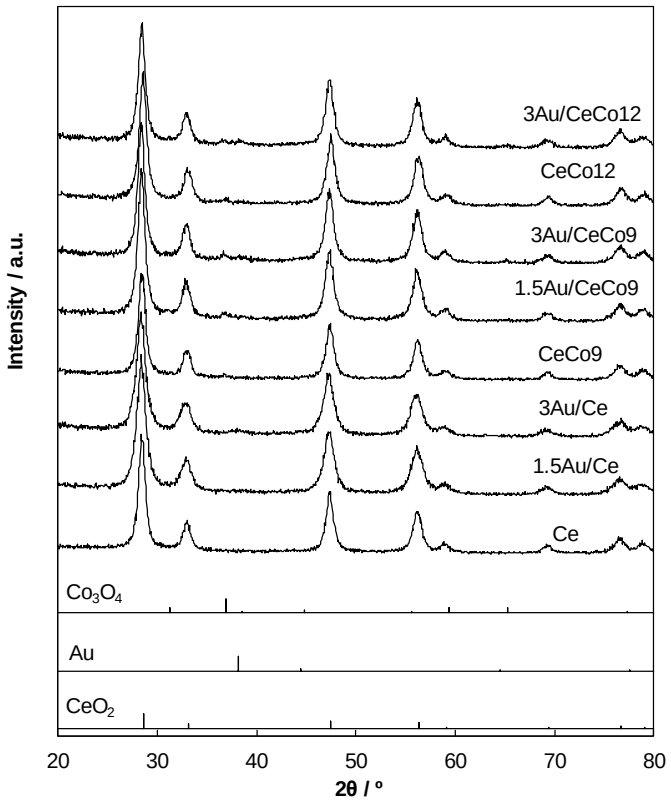


Figure 1 : XRD patterns of Ce, CeCox and yAu/CeCox samples

In order to get more insights into Au particle size and shape and as well on the representative morphology of $CeO_2$ and Co-promoted $CeO_2$ oxides, HR-TEM images were registered on two selected catalysts, 3Au/Ce and 3Au/CeCo9.
In Figure 2 two representative images are shown.

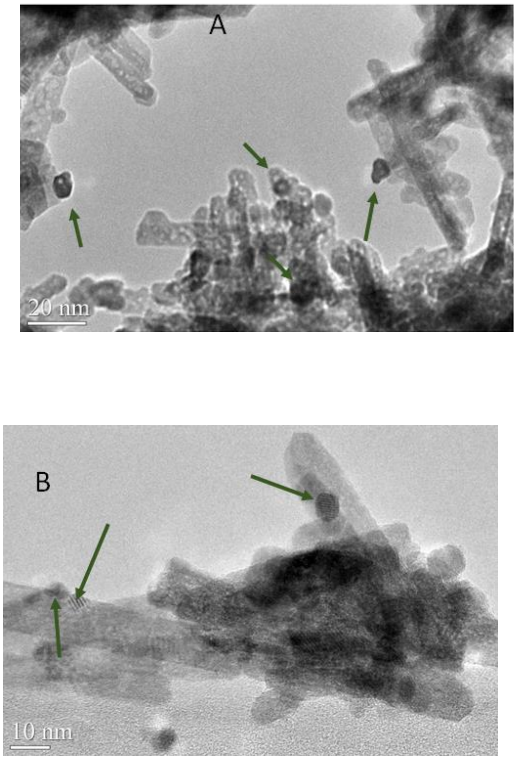


Figure 2: HRTEM images of (A) 3Au/Ce and (B) 3Au/CeCo9

Au nanoparticles around 5 nm were detected for 3Au/Ce (Figure 2A), while slightly smaller (3-5 nm) gold particles are found in the case of 3Au/CeCo9 (Figure 2 B). Moreover, according with the hydrothermal preparation method[28] used for the synthesis of the supports, the formation of $CeO_2$ nanorods (width around 5 nm and length in the range 30-100 nm) is well evident.
Raman spectroscopy was used first to characterize the nature of the ceria support. For sake of comparison along with the Micro Raman spectrum of the as-made ceria, that of a commercial $CeO_2$ (Aldrich) is also displayed in Figure 3. The two Raman spectra are dominated by a strong peak assigned to the vibrational mode of $F_{2g}$ symmetry in a cubic fluorite lattice. Interestingly, as compared to the Raman spectrum of the commercial $CeO_2$, the line shifts downwards (465 $cm^{-1}$ to 462 $cm^{-1}$), the line shape gets broader (FWMH $\times \approx$ 3) and asymmetric on the low-energy side appears clearly. These three features attest of the nanocrystallinity of the Ce support compared to the commercial $CeO_2$ sample[42]. Additionally, it is found some broad and ill-defined peaks located at about 260, 420, 480 and 600 $cm^{-1}$ in accordance with the literature[43]. The lines in the 480 $cm^{-1}$ - 600 $cm^{-1}$ wavenumber range were previously correlated to the presence of oxygen vacancies in ceria that are accompanied by the formation of reduced $Ce^{3+}$

sites[44,45,46]. The presence of lines in this energy range for Ce as compared to the commercial ceria indicates that smaller ceria particles possess an increased intrinsic capability towards oxygen vacancy formation. Recently an explanation for the origin of these experimentally observed lines within the 480–600 $cm^{-1}$ region has been reported based on calculated Raman spectra of reduced bulk ceria obtained from ab initio density functional theory (DFT) study of the vibrational properties of ceria[47]. The reduced model systems display signature vibrational lines in the 480–600 $cm^{-1}$ region associated with the presence of oxygen defects and reduced $Ce^{3+}$ ions. This study highlights that the spectral properties were strongly influenced by the coordination cubes around $Ce^{4+/3+}$ ions in $CeO_{2-x}$ [47]. A clear distinction was made between the Raman lines arising from $Ce^{3+}$ in direct proximity to the oxygen defect to those originating from $Ce^{3+}$ located in the second coordination sphere of the oxygen vacancy calculated at 500 $cm^{-1}$ and 480 $cm^{-1}$, respectively. Moreover, the 550 $cm^{-1}$ region can be also assigned to the $Ce^{3+}O_7V_O^{\bullet\bullet}$ coordination (i.e., $Ce^{3+}$ reduction close to a defect), whereas the 525 $cm^{-1}$ region is attributed to the $Ce^{4+}O_7V_O^{\bullet\bullet}$ coordination cube. However, in the 550 $cm^{-1}$ region as well as at higher wavenumbers, additional peaks with low intensity are predicted for all the coordination cubes around $Ce^{4+/3+}$ ions, which cannot be explained on the basis of the simple coordination model presented above.

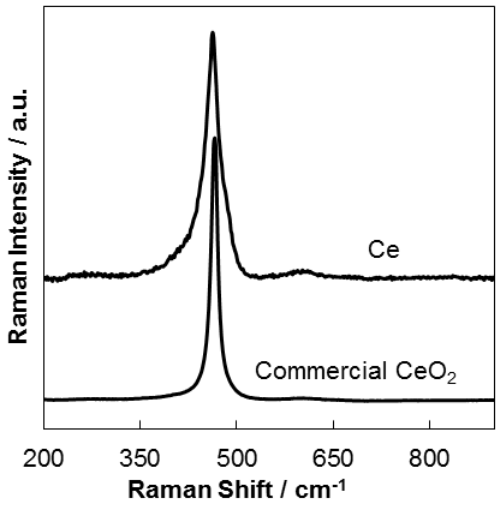


Figure 3 : Micro Raman spectra of the as made ceria (Ce) and of a commercial $CeO_2$

Figure 4 exhibits the macro-Raman spectra of Ce, CeCox and yAu/CeCox samples. To assess the influence of added Co ions on the structure of cerium oxide the Raman spectra of Ce and CeCo9 have been directly compared in Figure S4. We observed an increase of the shoulder at 490 $cm^{-1}$ for the Co-containing ceria which can be related to a mode of vibration associated with a $Ce^{3+}O_8$ cube. This observation can be related to an increase of oxygen vacancy density induced by partial incorporation of $Co^{3+}$ in the ceria lattice. However, the Raman spectra of all Co promoted $CeO_{2-x}$ exhibit an active Raman line at 693 $cm^{-1}$ which can be assigned to the presence of $Co_3O_4$. This is consistent with the micro Raman spectrum given in Figure S5. Thus, for some investigated grains, the characteristic Raman signature of $Co_3O_4$ can be clearly observed. The Raman spectrum exhibits five active Raman lines at 194, 480, 523, 618, and 693 $cm^{-1}$ in accordance with the literature[48]. The intensity ratio $I_{DEF}/I_{F2g}$ has been estimated, $I_{DEF}$ being the contribution of the Raman lines to ceria defect lines > 470 $cm^{-1}$ (Table 1). A direct comparison of the $I_{DEF}/I_{F2g}$ ratios shows that the density of $Ce^{3+}O_8$ polyhedrons increases with Co content. Furthermore, for a given Co content, it is also found a gold promotion effect on defective entities. The Raman spectra for yAu/CeCox samples indicate a more defective ceria consistent through the relative increase of intensity of the lines localized in the defect band regions 480-600 $cm^{-1}$. This indicates that gold promotes the density of $Ce^{3+}O_7V_O^{\bullet\bullet}$ and $Ce^{4+}O_7V_O^{\bullet\bullet}$ polyhedrons and even more when gold content increases (Table 1)[47]. It is worthy to note a line at 831 $cm^{-1}$ which may be attributed to nonplanar bridging peroxide species[49]. This result indicates that nanocrystalline $CeO_2$ stabilizes $O_2$ in part as peroxide species.

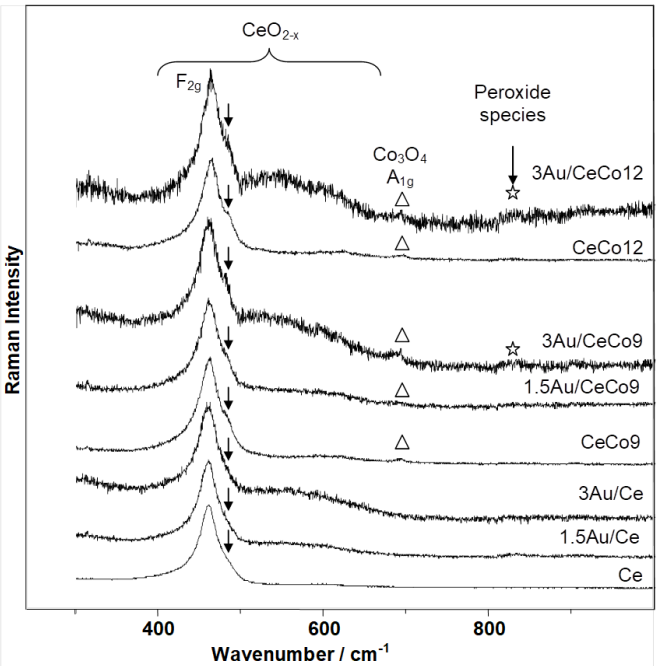


Figure 4 : Raman spectra of Ce, CeCox and yAu/CeCox samples

**Redox properties**

The $H_2$-TPR profiles of the supports are depicted in Figure S6 and hydrogen consumption are listed in Table 2. Pure ceria sample exhibits two main reduction regions denoted as medium temperature (MT) (200<T<600 °C) and high temperature (T>600 °C). The $H_2$ consumption centered at around 450°C corresponds to the $Ce^{4+}$ reduction from the uppermost layers, while the second one at higher temperature (centered at around 900°C) originates from the reduction of the bulk $CeO_2$[50]. Addition of cobalt to ceria modifies the $H_2$-TPR profiles. The reduction peak of the bulk ceria shifted to lower temperature (~800°C). The low temperature envelope between 200 and 400°C is similar to that obtained for the reduction of $Co_3O_4$. The small peak at around 250°C can be assigned to the reduction of $Co^{3+}$ to $Co^{2+}$, while the second one (around 300°C) originates from $Co^{2+}$ reduction to

$Co^0$ [51,52]. The shoulders of the peak at high temperature (320-400°C) could be assigned the reduction of the surface $CeO_2$. Therefore, in the presence of cobalt, the ceria (surface and bulk) reduction takes place at much lower temperature. This could be explained by a hydrogen spillover effect on metallic cobalt particles, which facilitates the ceria reduction[26]. It is found a decrease in the hydrogen consumption for CeCo12 in comparison with CeCo9 (Table 2) consistent with the increase in $Ce^{3+}$ density in agreement with Raman results. It is worth noting that $H_2$-TPR profiles obtained for CeCo9 and CeCo12 samples are similar to those obtained for $Co_3O_4$-$CeO_2$ catalysts prepared by impregnation of Co species over ceria support[53,54], confirming that the cobalt is mostly as $Co_3O_4$ phase.

Table 2 : $H_2$ consumption values obtained for Ce, CeCox and yAu/CeCox samples.

| Sample | LT* peak / mmol.$H_2$/$g^{-1}$ | MT** peak / mmol.$H_2$/$g^{-1}$ |
|---|---|---|
| Ce | - | 0.81 |
| CeCo9 | - | 1.48 |
| CeCo12 | - | 1.37 |
| 1.5Au/Ce | 0.81 | - |
| 3Au/Ce | 0.59 | - |
| 1.5Au/CeCo9 | 0.47 | 0.74 |
| 3Au/CeCo9 | 0.42 | 0.71 |
| 3Au/CeCo12 | 0.41 | 0.62 |

* Low Temperature ; ** Medium Temperature

The $H_2$-TPR profiles of the yAu/CeCox catalysts are depicted in Figure 5. For all samples an additional low temperature (LT) (T< 200 °C) $H_2$ consumption at ~85°C is observed. This contribution comes from the surface ceria reduction, which can be largely facilitated by the presence of metallic Au sites at the interface with ceria through a hydrogen spillover effect[50]. The hydrogen consumption is similar for pure ceria and 1.5 Au/Ce (Table 2). If we take into account the increase of $Ce^{3+}$ amount through gold loading (Raman results), the expected $H_2$ consumption should be less than that of 0.81 mmol.$H_2$/$g^{-1}$ registered for ceria alone. The observed value for 1.5Au/Ce can be explained by the presence of some additional reducible cationic gold species into the catalyst. For 3Au/Ce, the further decrease in $H_2$ consumption can be related to a more defective ceria structure as previously shown by Raman spectroscopy (Table 1). For Au/CeCox catalysts, the low temperature (LT) $H_2$ consumption values decrease in comparison with those of Au/Ce samples for Au loading of 1.5 wt% loading (Table 2) confirming the beneficial role of cobalt in the formation of oxygen vacancies directly connected to the $Ce^{3+}$ amount. Figure 6 shows the possible correlation between low temperature $H_2$ consumption and $I_{DEF}/I_{F2g}$ Raman ratio for yAu/CeCox samples. The low temperature $H_2$ consumption values linearly decrease with $I_{DEF}/I_{F2g}$ Raman ratio, confirming that the density increase of $Ce^{3+}O_7V_O^{\bullet\bullet}$ entities is responsible for the lower $H_2$ consumption at low temperature. Contrarily to Au/$CeO_2$, the $Co_3O_4$ reduction observed between 200°C and 350°C (MT peak), seems not to be affected by the presence of metallic Au in terms of peak position. The non-observance of $H_2$ spillover effect can be explained by the absence of a close interaction between Au sites and $Co_3O_4$. This assumption can be related to $Co_3O_4$ morphology effect in gold assisting $Co_3O_4$ reduction[55].

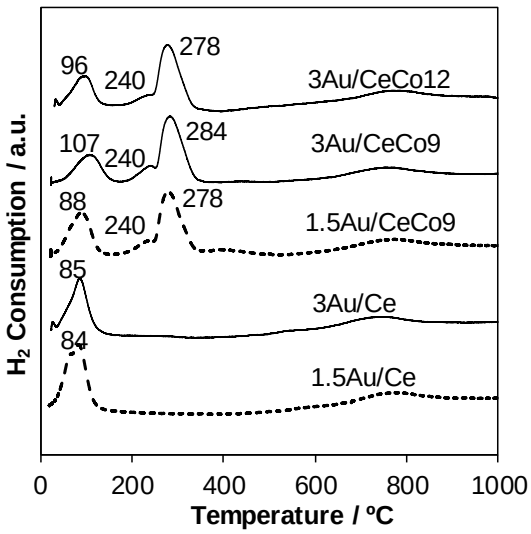


Figure 5 : $H_2$-TPR profiles of fresh yAu/CeCox samples

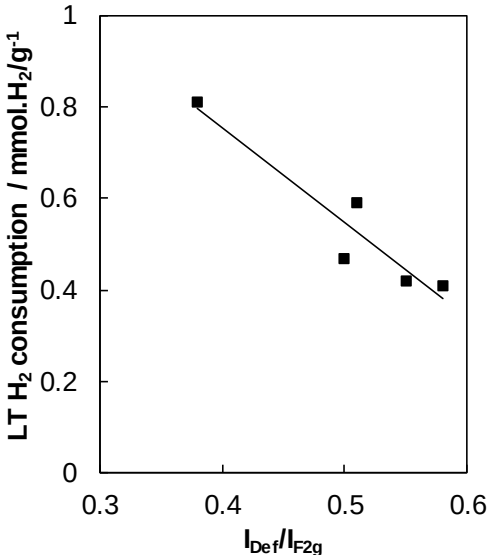


Figure 6 : LT $H_2$ consumption as a function of $I_{DEF}/I_{F2g}$ Raman ratio for yAu/CeCox samples

**Surface chemical properties**

The detailed XPS results obtained for the different samples are summarized in Table 3. The Ce 3d signal has a complex satellite structure due to hybridization between the Ce 4f and O 2p states. To estimate the surface ratios of $Ce^{3+}$ to the total amount of Ce species, the Ce 3d region has been fitted according to Burroghs *et al.*[56], with ten components that take into account the spin orbit splitting Ce$3d_{5/2}$ - Ce $3d_{3/2}$ and others splitting caused by a redistribution of the entire energy spectrum after a core hole is created (Figure S7). There are four peaks (labelled as $v^0$ $u^0$, $v^i$, $u^i$) attributed to $Ce^{3+}$ and six peaks (labelled as v, u, $v^{ii}$, $u^{ii}$, $v^{iii}$, $u^{iii}$) attributed to $Ce^{4+}$. The data were fitted using the constrains between the corresponding components $3d_{5/2}$- $3d_{3/2}$

given by Preisler *et al.*[57] All the supports showed analogous surface concentration of $Ce^{3+}$ species which increased in the corresponding Au catalysts (Table 3).

Table 3 : Summarized XPS results from Ce 3d and Au 4f core-level spectra

| Sample | $Ce^{3+}$ (%) | $Ce^{4+}$ (%) | Au $4f_{7/2}$ / eV | Au/Ce |
|---|---|---|---|---|
| Ce | 16 | 84 | - | - |
| 1.5Au/Ce | 21 | 79 | 85.3 | 0.05 (0.013) |
| 3Au/Ce | 19 | 81 | 85.3 | 0.09 (0.027) |
| CeCo9 | 15 | 85 | - | - |
| 1.5Au/CeCo9 | 15 | 85 | 85.0 | 0.05 (0.013) |
| 3Au/CeCo9 | 18 | 82 | 84.9 | 0.09 (0.027) |
| CeCo12 | 15 | 85 | - | - |
| 3Au/CeCo12 | 17 | 83 | 84.8 | 0.10 (0.027) |

The Au/Ce values in brackets correspond to the bulk ones

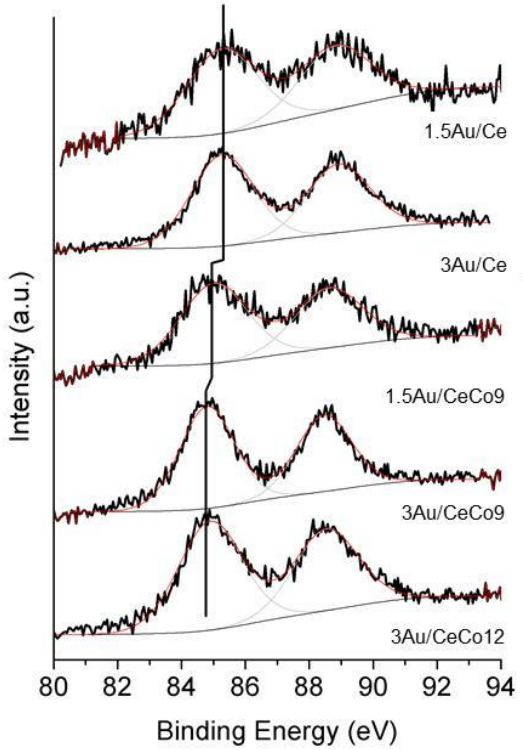


Figure 7 : XPS Au 4f signal obtained for yAu/CeCox

Au 4f region shows the two spin-orbit components Au $4f_{7/2}$ and Au $4f_{5/2}$ (Figure 7). The Au $4f_{7/2}$ BE values are listed in Table 3. The maximum of the Au $4f_{7/2}$ photopeak is located at 85.3 eV for Au/Ce samples, while it is located at lower BE (84.9 eV) for Au/CeCox samples. These BE values correspond to the presence of $Au^+$ species, without excluding the possibility of metallic gold to some extent. The observed decrease of BE values in the presence of Co is indicative of the presence of less oxidized gold and can be explained by a lowering of Au-$CeO_2$ interface.

The variations of the XPS Au/Ce atomic ratio are consistent with the increase of gold content in the sample. The larger XPS experimental values with respect to the bulk ones (Table 3) suggest that gold species are located on top the ceria nanoparticles. Moreover, the finding that the XPS Au/Ce atomic ratio measured for catalysts with Au 1wt % doubled for Au loading 3%, confirms comparable Au particle size for all the prepared catalysts.

Static ToF-SIMS has been used to probe the 3-4 outermost layers of the samples. Indeed, Static ToF-SIMS allows to get salient atomic and molecular information of the surface structure[58].

Table 4 : $AuO_2^-/Au^-$ and $CeO_2^+/CeO^+$ ratios extracted from ToF-SIMS spectra.

| Sample | Ce | CeCo9 | CeCo12 | 1.5Au/ Ce | 3Au/ Ce | 1.5Au/ CeCo9 | 3Au/ CeCo12 |
|---|---|---|---|---|---|---|---|
| $AuO_2^-/Au^-$ | - | - | - | 0.38 | 0.16 | 0.26 | 0.12 |
| $CeO_2^+/CeO^+$ | 0.014 | 0.014 | 0.011 | 0.013 | 0.011 | 0.015 | 0.011 |

Figure 8 shows the ToF-SIMS spectrum in the m/z (195-240) range obtained from the 1.5Au/CeCo9 sample. Along with the peak located at m/z = 197 assigned to $Au^-$ it is found secondary ions located at m/z = 213, 214, 229 and 230 assigned to $AuO^-$, $AuOH^-$, $AuO_2^-$ and $AuO_2H^-$, respectively. The detection of such entities evidences the presence of some oxidized gold in line with previous work[59]. Noteworthy, a decrease of the $AuO_2^-/Au^-$ ratio by a factor of about 2 both for ceria and Co promoted ceria supported gold catalysts is consistent with a decrease of the rate of oxidized gold with Au loading.

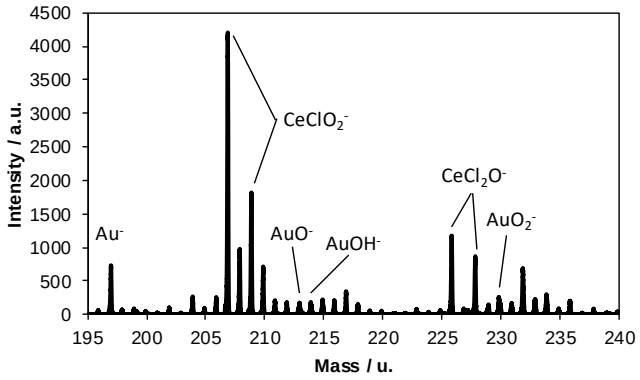


Figure 8 : Negative m/z (195-240) ToF-SIMS spectrum of the 1.5Au/CeCo9 sample

In order to investigate the role of cobalt and gold on oxygen defective $CeO_{2-x}$, the evolution of the $CeO_2^+/CeO^+$ ratio has been investigated as a function of the nature of the samples (Table 4). It is found a slight decrease of that ratio, indicative of a more defective ceria surface, with Co or/and Au addition and this decrease is all the more important than the Au(Co) content increases. Furthermore, ToF-SIMS studies reveal gold–ceria and cobalt-ceria interactions through the formation of secondary ions such as $CeAuO_2H^-$ and of $CoCeO_2^+$, $Ce_2CoO_4^+$, $Ce_3CoO_5^+$ and $Ce_4CoO_7^+$, respectively. Noteworthy no detection of $Au_xO_yCo_z^{\pm}$ ions is observed ruling out some possible interactions between Au and Co. This result is consistent with $H_2$-TPR results, suggesting the absence of interaction between Au and Co. Interestingly it is found the presence of the secondary ion $Co_3O_4^-$ (m/z = 240) in connection with the presence of the cobalt spinel oxide on both Co containing samples, in

agreement with XRD and Raman results. It should be noted that the $CeAuO_2^-/Au^-$ intensity ratio significantly decreases with Au content as shown in Figure S8 suggesting a decrease of gold-ceria interface related to the relative decrease of oxidized gold content.

The presence of chloride ions $Cl^-$ is also observed linked to the nature of the gold precursor which is $HAuCl_4$. Such observation using ToF-SIMS[60] is important knowing that chloride may have a great impact on the catalytic performances. The intensity ratio $Cl^-$/total allows to get information about the extent of chlorine contamination (Table S1). This ratio increases in the presence of gold content. The intensity ratio is about one order of magnitude higher for 1.5AuCe than for 3AuCe and rather similar features are observed for the Co-Au samples. As the magnitude but also the location of $Cl^-$ are of importance, possible direct interactions between $Cl^-$ and Ce, Co and Au have been investigated. It is worth to mention that the $CoCl^{\pm}$ secondary ions, contrarily to $AuCl^-$, are not observed. This clearly indicates the presence of chloride ions in the surrounding of gold centers. Decrease of $AuCl_2^-/Au^-$ intensity ratios from 1.5AuCe(Co) to 3.0AuCe(Co) indicates that the amount of gold bonded to $Cl^-$ increases with decreasing Au content. This is not accompanied with some agglomeration of gold as the $Au_4^-/Au^-$ intensity ratios keep lower for 1.5 Au wt% samples. No $Au_xCl_yO_z^{\pm}$ ions are detected suggesting that the presence of $Cl^-$ induces the formation of $AuCl_3$ entities, in line with the observation of $AuCl^-$, $AuCl_2^-$ and $AuCl_3^-$ ions (in m/z) at 232, 267 and 302, respectively. The reverse correlation has to be made when considering the $CeCl_2^+/Ce^+$ intensity ratios. Regarding Co, formation of oxichlorocobalt species may be expected consistent with the detection of CoOCl ions.

**Catalytic properties**

The HCHO light-off curves for the prepared supports are shown in Figure S9. The pure ceria support is poorly active, reaching 40% HCHO conversion into $CO_2$ at 300°C. However, doping $CeO_2$ with Co enhances significantly the catalytic activity and whatever the cobalt content the total conversion of formaldehyde is obtained at 250°C. The higher activity in HCHO oxidation of CoCe oxides in comparison with that of pure $CeO_2$ could be explained by the higher redox properties of the composite due to the combination of the redox properties of both oxides, *i.e.* the reduction of $Co_3O_4$ and the assisted reduction of $CeO_2$ at the vicinity of cobalt species, as suggested by $H_2$-TPR analysis. Indeed, studying pure $Co_3O_4$, Z. Fan *et al.*[61] proposed that $Co^{3+}$ ions are active sites for total formaldehyde oxidation. Dioxygen can be activated over ceria oxygen vacancies[62]. Therefore, it can be proposed that $Co^{3+}$ may be reduced by HCHO into $Co^{2+}$, while activated oxygen transforms $Ce^{3+}$ into $Ce^{4+}$. A continuous oxygen transfer from $CeO_2$ to CoO could occur through the synergistic effect between $CeO_2$ and $Co_3O_4$ illustrated in Scheme S1. The HCHO light-off curves for the Au/Ce and Au/CeCo catalysts are shown in Figure 9A. A remarkable HCHO oxidation activity improvement is observed when Au is added to the supports, full conversion being achieved at around 100 °C for all catalysts. For $Au/CeO_2$ samples, the two-fold gold content increase allows to raise the HCHO conversion into $CO_2$ from 20% to 90% at 25°C, respectively. Starting from 60°C, the difference in conversion is much less pronounced owing to the significant increase of HCHO oxidation in the temperature range 20-60°C in the presence of Au1.5/Ce catalyst (Figure 9A). The effect of gold loading in formaldehyde oxidation has already been addressed by several authors. Regardless of the support used, $ZrO_2$[14], FeOx[13], $CeO_2$[27], it is generally pointed out that increasing gold content results in catalytic performance enhancement in formaldehyde oxidation. The addition of slight amounts of Co (9 or 12 mol %) notably boosts the formaldehyde conversion of the $Au/CeO_2$ materials. The results are especially impressive using lower gold content (1.5 wt%) since 80% of HCHO conversion at 25°C is obtained for 1.5Au/CeCo9, while the unmodified 1.5Au/Ce catalyst achieved the same conversion at around 60°C. Lakshmanan *et al.*[62] shown that gold nanoparticles enhanced the oxygen storage capacity and the rate of oxygen exchange and promoted the activation of dioxygen by generating $O_2^{2-}$ species at the gold/ceria interface perimeter. This result is consistent with the observance of peroxo species ($O_2^{2-}$) by Raman spectroscopy for 3Au/CeCox samples.

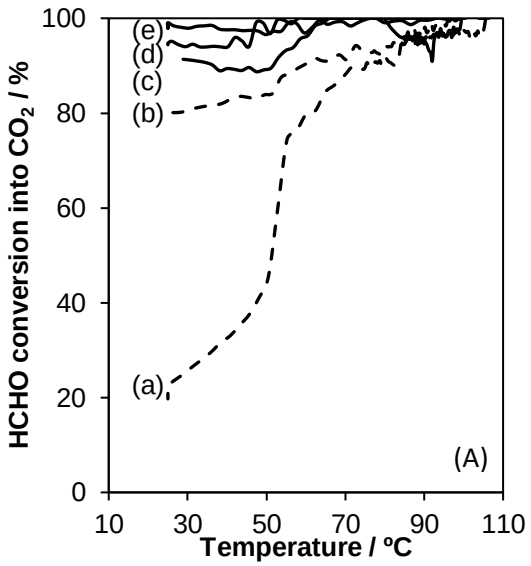

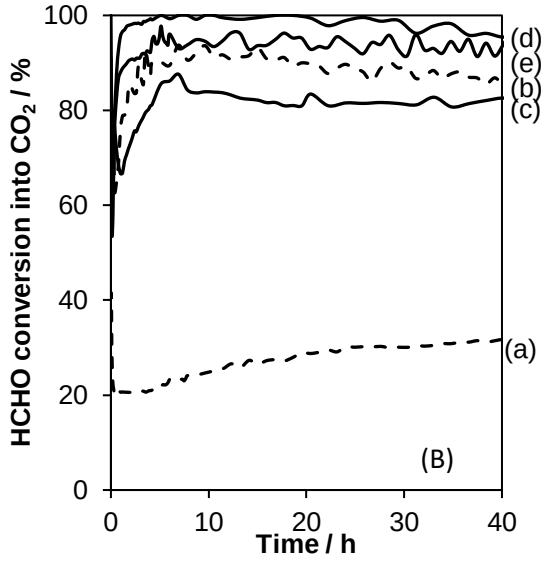


Figure 9 : HCHO conversion into $CO_2$ for the (a) 1.5Au/Ce ; (b) 1.5Au/CeCo9 ; (c) 3Au/Ce ; (d) 3Au/CeCo12 and (e) 3Au/CeCo9 catalysts (A) as a function of the decreasing temperature ; (B) at 25°C for 40h

The durability tests over Au related catalysts are shown in Figure 9B. It is observed an increase of the HCHO conversion in the first hours of the test, except for the 1.5Au/Ce catalyst, for which the conversion always increases with time but at a lower rate. This induction period can be related to the reactive desorption of chemically intermediate species resulting from the partial oxidation of HCHO such as formates. After that induction period, the HCHO conversion into $CO_2$ with time keeps rather stable or decreases to a less extent with time.

The HCHO conversion obtained at t = 0 h increases with the Raman ratio $I_{DEF}/I_{F2g}$ (Table 1). This clearly shows the beneficial role of oxygen vacancies in HCHO total oxidation. The positive role of cobalt in the formation of oxygen vacancies can be the cause of better activity. The increase of defects in ceria is highlighted by the increase of $Ce^{3+}O_7V_O^{\bullet\bullet}$ entities (Raman analysis) and by the increasing amount of $Ce^{3+}$ species in line with lower $H_2$ consumption amounts observed on $H_2$-TPR by adding Co. It is well known that oxygen vacancies allow higher oxygen mobility and formation of oxygen active species that can improve oxidation of reaction intermediates. The correlation between HCHO conversion into $CO_2$ and the $I_{DEF}/I_{F2g}$ Raman ratio clearly supports the fact that the amount of oxygen vacancy plays a critical role HCHO total oxidation.

The catalyst activity was compared in terms of activity expressed as µmole of HCHO converted into $CO_2$ per second and per gram of Au, after 40h of testing. The data are compared to those obtained at t = 0 h and are also listed in Table 5.

Table 5 : Catalytic results of HCHO oxidized at 25 °C

| Catalysts | Activity* /µmol.s$^{-1}$.gAu$^{-1}$ | |
|---|---|---|
| | t = 0 | t = 40 h |
| 1.5Au/Ce | 0.9 | 1.5 |
| 3Au/Ce | 1.6 | 1.9 |
| 1.5Au/CeCo9 | 2.9 | 3.9 |
| 3Au/CeCo9 | 1.2 | 2.2 |
| 3Au/CeCo12 | 1.5 | 2.2 |

* activity measured at 25°C

As reported in Table 5, all catalysts exhibit similar activities of about 2 µmol.s$^{-1}$.gAu$^{-1}$ except for 1.5Au/CeCo9 which displays a two-fold activity, namely 3.9 µmol.s$^{-1}$.gAu$^{-1}$ at 40 h. The absence of gold dispersion modification revealed by XPS data between 1.5Au/Ce and 1.5Au/CeCo9 samples cannot explain this improvement in activity. By opposition the increase of gold ceria interface, promoting oxygen vacancy, relied to a more oxidized gold species are recognised herein to be key parameters for increasing activity over the 1.5Au/CeCo9 sample.

## Conclusions

The effect of Co incorporation into Au/$CeO_2$ based catalysts has been investigated by varying the Co and Au content. The catalytic performances in HCHO oxidation were herein discussed in line with the physico-chemical characterizations of the fresh catalysts. BET, XRD, Raman and TPR characterization performed on Au/Co-promoted ceria catalysts suggested that cobalt is mostly as $Co_3O_4$ phase, while no direct evidences of Co ions insertion into the $CeO_2$ lattice were found by XRD. HRTEM images evidenced the presence of Au particles around 5 nm and as well the formation of $CeO_2$ nanorods. High dispersion of Au particles on the ceria top and comparable Au size for all the prepared catalysts were confirmed by the XPS analysis.

A beneficial role of cobalt in the formation of oxygen vacancies directly connected to the $Ce^{3+}$ amount was evidenced by Raman and TPR. The oxygen vacancies formed play a double role in enhancing the HCHO catalytic activity of Au/Co-promoted $CeO_2$ catalysts: $Ce^{3+}$ ions represent nucleation centers for the stabilization of active Au ionic species and, at the same time, gaseous oxygen is easily activated over such centers. The presence of close gold–ceria and cobalt-ceria interaction was further confirmed by ToF-SIMS studies, while no detection of $Au_xO_yCo_z^{\pm}$ ions was observed ruling out some possible Au-Co contact.

## Conflicts of interest

There are no conflicts to declare.

## Acknowledgements

Leonarda Francesca Liotta thanks the University of Lille for the visiting professor position. This research is partially supported by a French-Italian project (PHC Galilée N°39624UG) and by an European Program INTERREG V France—Wallonie—Flanders

(FEDER) (DepollutAir). Chevreul Institute (FR 2638), Ministère de l'Enseignement Supérieur et de la Recherche and Région Hauts-de-France are also acknowledged for supporting this work.

The authors thank Jean-Charles Morin, Nicolas Nuns, Olivier Gardoll, Christine Lancelot and Laurence Burylo for their contribution in Raman, ToF-SIMS, $H_2$-TPR, HRTEM and XRD measurements, respectively.

## Notes and references

1 IARC, *IARC (International Agency Res. Cancer)*, 1982, **29**.
2 J. Q. Torres, S. Royer, J. P. Bellat, J. M. Giraudon and J. F. Lamonier, *ChemSusChem*, 2013, **6**, 578–592.
3 G. Zhang, Y. Hong and W. He, Indoor Built Environ., 2015, **24**, 138–144.
4 L. Qi, B. Cheng, J. Yu and W. Ho, *J. Hazard. Mater*., 2016, **301**, 522–530.
5 H. Tan, J. Wang, S. Yu and K. Zhou, *Environ. Sci. Technol*., 2015, **49**, 8675–8682.
6 G. Pang, D. Wang, Y. Zhang, C. Ma and Z. Hao, *Front. Environ. Sci. Eng*., 2016, **10**, 447–457.
7 M. HARUTA, *J. Catal*., 1989, **115**, 301–309.
8 B. Chen, X. Zhu, Y. Wang, L. Yu and C. Shi, *Chinese J. Catal*., 2016, **37**, 1729–1737.
9 S. Scirè and L. F. Liotta, *Appl. Catal. B Environ*., 2012, **125**, 222–246.
10 Z. Tang, W. Zhang, Y. Li, Z. Huang, H. Guo, F. Wu and J. Li, *Appl. Surf. Sci*., 2016, **364**, 75–80.
11 B.-B. Chen, X.-B. Zhu, Y.-D. Wang, L.-M. Yu, J.-Q. Lu and C. Shi, *Catal. Today*, 2017, **281**, 512–519.
12 B. B. Chen, C. Shi, M. Crocker, Y. Wang and A. M. Zhu*, Appl. Catal. B Environ*., 2013, **132–133**, 245–255.
13 C. Li, Y. Shen, M. Jia, S. Sheng, M. O. Adebajo and H. Zhu, *Catal. Commun*., 2008, **9**, 355–361.
14 Y. C. Hong, K. Q. Sun, K. H. Han, G. Liu and B. Q. Xu, *Catal. Today*, 2010, **158**, 415–422.
15 Y. Shen, X. Yang, Y. Wang, Y. Zhang, H. Zhu, L. Gao and M. Jia, *Appl. Catal. B Environ*., 2008, **79**, 142–148.
16 Y. Wang, B. B. Chen, M. Crocker, Y. J. Zhang, X. B. Zhu and C. Shi, *Catal. Commun*., 2015, **59**, 195–200.
17 C. Ma, G. Pang, G. He, Y. Li, C. He and Z. Hao, *J. Environ. Sci. (China),* 2016, **39**, 77–85.
18 B. bing Chen, X. bing Zhu, M. Crocker, Y. Wang and C. Shi, *Appl. Catal. B Environ*., 2014, **154–155**, 73–81.
19 M. Jia, Y. Shen, C. Li, Z. Bao and S. Sheng, *Catal. Letters*, 2005, **99**, 235–239.
20 M. Jing, W. Song, L. Chen, S. Ma, J. Deng, H. Zheng, Y. Li, J. Liu and Z. Zhao, *J. Phys. Chem. C*, 2018, **122**, 438–448.
21 C. T. Campbell and C. H. F. Peden, *Science*, 2005, **309**, 713-714.
22 R. Brezny, T. Egami, E. Mamontov, S. Tyagi and M. Koranne, *J. Phys. Chem. B*, 2002, **104**, 11110–11116.
23 T. X. T. Sayle, S. C. Parker and C. R. A. Catlow, *Surf. Sci*., 1994, **316**, 329–336.
24 X. Liu, K. Zhou, L. Wang, B. Wang and Y. Li, J. Am. *Chem. Soc*., 2009, **131**, 3140–3141.
25 B. Liu, C. Li, Y. Zhang, Y. Liu, W. Hu, Q. Wang, L. Han and J. Zhang, *Appl. Catal. B Environ*., 2012, **111–112**, 467–475.
26 Y. Liu, B. Liu, Q. Wang, C. Li, W. Hu, Y. Liu, P. Jing, W. Zhao and J. Zhang, *J. Catal*., 2012, **296**, 65–76.
27 J. Zhang, Y. Jin, C. Li, Y. Shen, L. Han, Z. Hu, X. Di and Z. Liu, *Appl. Catal. B Environ*., 2009, **91**, 11–20.
28 Q. Xu, W. Lei, X. Li, X. Qi, J. Yu, G. Liu, J. Wang and P. Zhang, *Environ. Sci. Technol*., 2014, **48**, 9702–9708.
29 H. F. Li, N. Zhang, P. Chen, M. F. Luo and J. Q. Lu, *Appl. Catal. B Environ*., 2011, **110**, 279–285.
30 C. Ma, D. Wang, W. Xue, B. Dou, H. Wang and Z. Hao, *Environ. Sci. Technol*., 2011, **45**, 3628–3634.
31 B. Liu, Y. Liu, C. Li, W. Hu, P. Jing, Q. Wang and J. Zhang, *Appl. Catal. B Environ*., 2012, **127**, 47–58.
32 M. N. Revoy, R. W. J. Scott and A. P. Grosvenor, *J. Phys. Chem. C*, 2013, **117**, 10095–10105.
33 O. H. Laguna, F. R. Sarria, M. A. Centeno and J. A. Odriozola, *J. Catal*., 2010, **276**, 360–370.
34 S. Yabe, M. Yamashita, S. Momose, K. Tahira, A. Yoshida, R. Li, S. Yin and T. Sato, *Int. J. Inorg. Mater*., 2001, **3**, 1003–1008.
35 Y. A. S. Khadar, A. Balamurugan, V. P. Devarajan, R. Subramanian and S. D. Kumar, *Integr. Med. Res*., 2018, 1–8.
36 S. Akram, Z. Wang, L. Chen, Q. Wang, G. Shen, N. Han, Y. Chen and G. Ge, *Catal. Commun*., 2016, **73**, 123–127.
37 N. S. Arul, D. M. Pao and C. Chen, *J. sol-Gel Sci. Technol*., 2012, **64**, 515–523.
38 R. D. Shannon, *Acta Crystallogr. Sect. A*, 1976, **32**, 751–767.
39 W. E. Mahmoud, A. A. Al-Ghamdi, F. A. Al-Agel, E. Al-Arfaj, F. S. Shokr, S. A. Al-Gahtany, A. Alshahrie, O. Jalled, L. M. Bronstein and G. W. Beall, *Mater. Res. Bull*., 2015, **72**, 154–159.
40 R. Murugan, G. Vijayaprasath, T. Mahalingam and G. Ravi, *Ceram. Int*., 2016, **42**, 11724–11731.
41 L. U. Suhong, W. Fan, C. Canchang, H. Fenglin and L. I. Kelun, *J. Rare Earths*, 2017, **35**, 867–874.
42 J. E. Spanier, R. D. Robinson, F. Zhang, S.-W. Chan and I. P. Herman, *Phys. Rev. B*, 2001, **64**, 245407.
43 J. Guzman, S. Carrettin and A. Corma, *J. Am. Chem. Soc*., 2005, **127**, 3286–3287.
44 J. R. McBride, K. C. Hass, B. D. Poindexter and W. H. Weber*, J. Appl. Phys*., 1994, **76**, 2435–2441.
45 T. Taniguchi, T. Watanabe, N. Sugiyama, A. K. Subramani, H. Wagata, N. Matsushita and M. Yoshimura, *J. Phys. Chem. C*, 2009, 1**13**, 19789–19793.
46 Z. Wu, M. Li, D. R. Mullins and S. H. Overbury, *ACS Catal*., 2012, **2**, 2224–2234.
47 C. Schilling, A. Hofmann, C. Hess and M. V. Ganduglia-Pirovano, *J. Phys. Chem. C*, 2017, **121**, 20834–20849.
48 V. G. Hadjiev, M. N. Iliev and I. V Vergilov, *J. Phys. C Solid State Phys*., 1988, **21**, L199–L201.
49 Y. Lee, G. He, A. J. Akey, R. Si, M. Flytzani-stephanopoulos and I. P. Herman, *J. Am. Chem. Soc*., 2011, **133**, 12952–12955.
50 Y. Liu, B. Liu, Y. Liu, Q. Wang, W. Hu, P. Jing, L. Liu, S. Yu and J. Zhang, *Appl. Catal. B Environ*., 2013, **142–143**, 615–625.
51 S. S.-Y. Lin, D. H. Kim, M. H. Engelhard and S. Y. Ha, *J. Catal*., 2010, **273**, 229–235.
52 P. Gawade, B. Bayram, A. M. C. Alexander and U. S. Ozkan, *Appl. Catal. B Environ*., 2012, **128**, 21–30.
53 J. Y. Luo, M. Meng, X. Li, X. G. Li, Y. Q. Zha, T. D. Hu, Y. N. Xie and J. Zhang, *J. Catal*., 2008, **254**, 310–324.
54 J. Dou, Y. Tang, L. Nie, C. M. Andolina, X. Zhang, S. House, Y. Li, J. Yang and F. (Feng) Tao, *Catal. Today*, 2018, **311**, 48–55.
55 Y. Yao, L. L. Gu, W. Jiang, H. C. Sun, Q. Su, J. Zhao, W. J. Ji and C. T. Au, *Catal. Sci. Technol*., 2016, **6**, 2349–2360.
56 P. Burroughs, A. Hamnett, A. F. Orchard and G. Thornton, *J. Chem. Soc. Dalt. Trans*., 1976, **17**, 1686.
57 E. J. Preisler, O. J. Marsh, R. A. Beach and T. C. McGill, *J. Vac. Sci. Technol. B Microelectron. Nanom. Struct*., 2001, **19**, 1611.
58 L. T. Weng, *Appl. Catal. A Gen*., 2014, **474**, 203–210.
59 L. Fu, N. Q. Wu, J. H. Yang, F. Qu, D. L. Johnson, M. C. Kung, H. H. Kung and V. P. Dravid, *J. Phys. Chem. B*, 2005, **109**, 3704–3706.
60 I. Dobrosz-Gómez, I. Kocemba and J. M. Rynkowski, *Appl. Catal. B Environ*., 2009, **88**, 83–97.
61 Z. Fan, W. Fang, Z. Zhang, M. Chen and W. Shangguan*, Catal. Commun*., 2018, **103**, 10–14.
62 P. Lakshmanan, F. Averseng, N. Bion, L. Delannoy, J. M. Tatibouët and C. Louis, *Gold Bull*., 2013, **46**, 233–242.